Structural features of defect cascades in $YBa_2Cu_3O_x$ as a function of oxygen stoichiometry

By B. G. STOREY†, M. A. KIRK‡, J. A. OSBORNE§, L. D. MARKS†,
P. KOSTIC‡ and B. W. VEAL‡

†Materials Science and Engineering, Northwestern University, Evanston, Illinois
60208, USA
‡Materials Science Division, Argonne National Laboratory, Argonne, Illinois
60439, USA
§Department of Statistics, Northwestern University, Evanston, Illinois 60208,
USA

ABSTRACT

Single crystals of $YBa_2Cu_3O_x$, of various oxygen stoichiometries, were irradiated with 50 keV Kr^+ to create defect cascades similar to those resulting from fast neutron irradiation. Two-beam dark-field transmission electron microscopy in weak dynamic conditions was used to measure the defect cascade size distribution in the principal axes for four different oxygen stoichiometries, and high-resolution electron microscopy verified the mean size of these cascades. The mean size of the defect cascades generated was independent of oxygen stoichiometry from $x = 6.35$ to $x = 6.9$, which indicates that magnetic flux pinning does not vary because of any association between the oxygen concentration and the cascade size. For Kr^+ incident near the c axis the defect cascades have on average a circular cross-section of 3·5 nm diameter perpendicular to the ion beam, while an elliptical cross-section was found for ions incident near the x axis. The minor axis (3·5 nm) was in the [001] direction and the major axis (5·5 nm) was in the [010] direction. This aspect ratio of 1·6 matches that found for high-energy heavy-ion track damage in $YBa_2Cu_3O_x$, which implies that the shape is determined not by the recoil damage mechanism but in the cooling or relaxation stage where the anisotropy in thermal conductivity determines the defect shape.

§ 1. INTRODUCTION

Irradiation-damage-induced defects enhance the critical current density J_c of superconductors by providing effective pinning centres for magnetic vortices. In the attempt to maximize J_c, many forms of irradiation have been employed: electrons (Giapintzakis et al. 1992), protons (Civale et al. 1990, Kirk 1993), neutrons (Lessure et al. 1991, Vlcek et al. 1992) and ions (Civale et al. 1991, Budhani, Zhu and Suenaga 1992). Depending upon the energy and mass of the bombarding particle a wide variety of defects are generated. Electrons and light ions produce predominately Frenkel pairs and clusters of vacancies or interstitials. Fast neutrons produce a range of damage mechanisms dominated by cascades and smaller cluster defects (Vlcek et al. 1992, Frischherz et al. 1994). Gigaelectronvolt ions leave continuous tracks of damage greater than several microns in length (Wheeler et al. 1993). Knowing the defect structure of tracks, cascades or small clusters of interstitials or vacancies is important in relating a defect type to its flux pinning properties.

Molecular dynamic calculations for 100–300 eV oxygen, copper, yttrium and barium ion damage in $YBa_2Cu_3O_x$ (YBCO) predict an increase in defect cascade size with decreasing oxygen concentration (Kirsanov, Muslin, Roskin and Shamarina 1993). Oxygen stoichiometries $x = 7 \cdot 0$, $6 \cdot 5$ and $6 \cdot 0$ were studied and average defect cascade sizes of $2 \cdot 7$, $3 \cdot 8$ and 6 nm respectively were calculated. This size variation was attributed to oxygen atoms acting as a viscous medium to reduce the lengths of replacement collision sequences. It was proposed that the smaller cascades with more localized damage produced in the higher oxygen concentration are more effective pinning centres.

Intragrain flux pinning measurements made on fast-neutron-irradiated YBCO ceramics for both the 60 and 90 K T_c phases revealed a difference in J_c enhancement between the 60 and 90 K phases (Wisniewski *et al.* 1994). The natural question that this difference raises involves the defect cascade size distribution in each phase. An assumption that the defect cascade size was larger in the more oxygen-deficient YBCO (60 K T_c) was coupled with the coherence length differences between the two phases and at different measuring temperatures to explain the flux-pinning data. They based their assumption of cascade size on theoretical work involving low-energy recoils (Kirsanov, Musin and Wisniewski 1993).

Direct size measurements, using high-resolution electron microscopy (HREM), of amorphous tracks resulting from 300 MeV Au^{24+} show a size anisotropy in YBCO (Zhu *et al.* 1993). The cross-section of the tracks along the [001] direction is smaller than that of tracks along the [100] direction. Also the tracks along the [001] direction are circular while the tracks along the [100] direction are elliptical with the major axis along the [010] direction. This was explained to the first approximation by a thermal spike model coupled with the anisotropy of the thermal conductivity in YBCO (Hagen, Wang and Ong 1989, Shao-Chun *et al.* 1991). However, the size anisotropy, which had an aspect ratio of $1 \cdot 6$ for the a- to c-axis dimensions, is much less than the ratio of 3–5 that is predicted by the thermal conductivity anisotropy.

A thorough transmission electron microscopy (TEM) study of the cascade microstructure resulting from 50 and 85 keV Kr^+ and Xe^+ irradiation of the 90 K phase of YBCO has been reported (Frischherz, Kirk, Zhang and Weber 1993). It was found that the defect cascades produced had a cross-section approximately $3 \cdot 5$ nm in diameter. Recrystallization of cascades was suggested due to a 50% yield of defect cascades per incident ion and apparent lattice fringes in the centre of a HREM image of a cascade. The present paper addresses the size distribution and anisotropy of 50 keV Kr^+ irradiation induced defect cascades in YBCO as a function of oxygen stoichiometry.

§ 2. EXPERIMENTAL

Single crystals of YBCO were grown at Argonne National Laboratory in gold crucibles by the self-flux method (Kaiser, Holtzberg, Chisholm and Worthington 1987) and had typical sizes of 1 mm × 1 mm × $0 \cdot 1$ mm. The crystals were oxygenated to $x = 6 \cdot 9$ in flowing oxygen at 480°C for 3 days, furnace cooled to 420°C, held there for another 5 days and finally furnace cooled to room temperature. Several crystals were reoxygenated, using procedures described previously (Veal *et al.* 1990), to obtain a range of oxygen concentrations: $x = 6 \cdot 9$, $6 \cdot 7$, $6 \cdot 55$ and $6 \cdot 35$. To determine the values of T_c, magnetization measurements against temperature were made using a low-field superconducting quantum interference device (SQUID). The data in fig. 1

Fig. 1
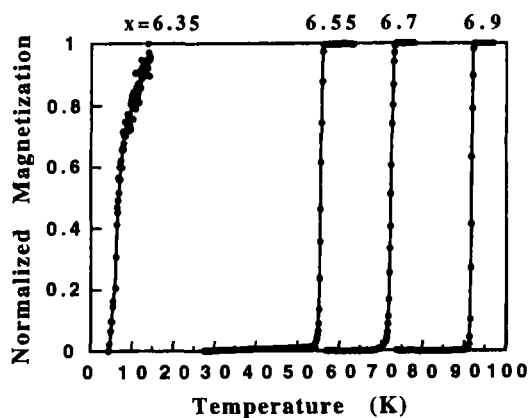
Low-field dc SQUID magnetization curves of the four YBCO single crystals used in this experiment. The narrow transition width from the normal to superconducting state implies that the crystals are single phase and the oxygen concentration is homogeneous. The transition temperature is used to determine the average oxygen stoichiometry, indicated above each curve.

show very sharp transitions, typically less than 2 K, which indicate single-phase crystals with nearly uniform oxygen stoichiometry.

TEM samples were prepared by crushing a single crystal in two drops of anhydrous methanol and dispersing it onto a clean one thousand mesh TEM grid; storage was under static dry nitrogen. This procedure reduced sample damage compared with ion milling or chemical polishing (St Louis-Weber, Dravid and Balachandran 1995) and reduced the exposure to the deleterious effects of water (Marks, Li, Shibahara and Zhang 1988, van Tendeloo and Amelinckx 1988).

Prior to irradiating the crushed YBCO crystals, a region of the TEM grid containing thin clean crystals with favourable orientations was located. The radiation was performed in the HVEM–Tandem Facility at Argonne National Laboratory (Allen, Funk, Ryan and Taylor 1989) with the ion beam centred on the aforementioned region. Dosimetry was done with a Faraday cup for which calibration had been performed earlier (Vetrano 1990). A National Electronics Corporation ion implanter delivered 50 keV Kr^+ through an ion beam interface into the sample area of the high voltage electron microscope. A fluence of 2×10^{11} ions cm^{-2} was used so that the defect density would be sizeable but without significant overlap. To avoid confusion the following notation for ion direction and size measurement direction will be used in this paper; the ion direction will be near the a, b or c axis and measurements will be $[010]_a$, $[001]_a$, $[010]_c$ and $[110]_c$, where the subscript indicates the incident ion direction. In this notation the b axis is coincident with the CuO chains and the c axis is in the long (1·168 nm) unit-cell dimension.

All TEM data were collected at 100 keV which is below all damage threshold energies except one planar oxygen site (O(2)) when the electron beam is near the a, b or c axes (Kirk *et al.*, 1988, Basu, Roy, Mitchell and Nastasi 1989, Kirsanov, Musin and Shamarina 1992, Kirsanov, Musin and Shamarina 1994). HREM images were obtained using a Hitachi H-9000, while dark-field images and diffraction patterns

were obtained using a Philips CM30. An Optronics P1000 densitometer was used to digitize the TEM negatives to eight bits with a linear distribution of optical densities between zero and two; the images were analysed with SEMPER 6 image processing software. A Wiener filter (Marks 1995) was used to remove the shot noise from the HREM images, that is an estimate of the noise in the power spectrum was removed from the amplitude component of the Fourier transform.

The defect cascade size was measured by viewing the digitized dark-field negatives at a magnification of about 1·5 million, with a pixel on the computer monitor equal to 0·15 nm. The line of no contrast (black–white interface) was taken as the diameter for cascades showing black–white contrast (Ashby and Brown 1963), while the width perpendicular to g was measured for cascades showing black dot contrast (Wilkens 1970). The length of the black–white interface is only weakly dependent on the deviation from the exact Bragg condition (Saldin, Stathopoulos and Whelan 1979).

Measuring the defect cascade density was achieved by printing the original dark-field image negatives to a total magnification of about 500 000 and selecting an area with good defect contrast. The cascades clearly showing black–white contrast were counted as one, and cascades with less pronounced black–white or black dot contrast as one half (Frischherz *et al.* 1993). This is due to the difficulty in distinguishing between surface artefacts and cascades showing weak contrast. The total error was assigned as one half the black dot density plus a 10% error in the ion fluence (Vetrano 1990).

§ 3. EXPERIMENTAL RESULTS

Dark-field imaging in weak dynamic conditions, usually (g, 1·25g), was used to image the Kr^+ defect cascades; for instance see fig. 2. The [200], [020] and [006] reflections were used from the a and c zone axes, thereby enabling size measurements in the $[100]_c$, $[010]_c$, $[010]_a$ and $[001]_a$ directions. Size measurements were made by measuring both the black–white interface length and the width perpendicular to g of black dot features. Simultaneous 95% confidence intervals were generated according to Scheffé's procedure to determine any trends present (table). Except for the larger $[010]_a$ size measured with the [006] reflection, the means all lie within 0·8 nm. A difference of at least 0·2 nm between any two means is statistically significant at the 95% confidence level.

The data for $x = 6.9$ when plotted (fig. 3) show the size distribution in all three directions for the two zone axes studied. The defect cascades produced from ions incident near the c axis have a circular cross-section, while an elliptical-cross section was found for ions incident near the a axis. The plots in fig. 4 show the $[010]_c$ size distribution in each of the four oxygen stoichiometries studied and demonstrate that the defect cascade size is independent of oxygen content. The size distributions for $[100]_c$ and $[001]_a$, not shown, have the same overall shape and mean as those in fig. 4. As each defect size measurement was made, a record was kept as to whether the defect showed black–white or black dot contrast. The combined data for all size directions and oxygen stoichiometries, excluding the larger $[010]_a$ data, for the black–white and black dot contrast are shown in fig. 5. The overall shapes of the distributions are nearly identical and the shift in peaks is small (0·3 nm); therefore defect showing either black–white or black dot contrast were sized to improve the statistics.

Fig. 2
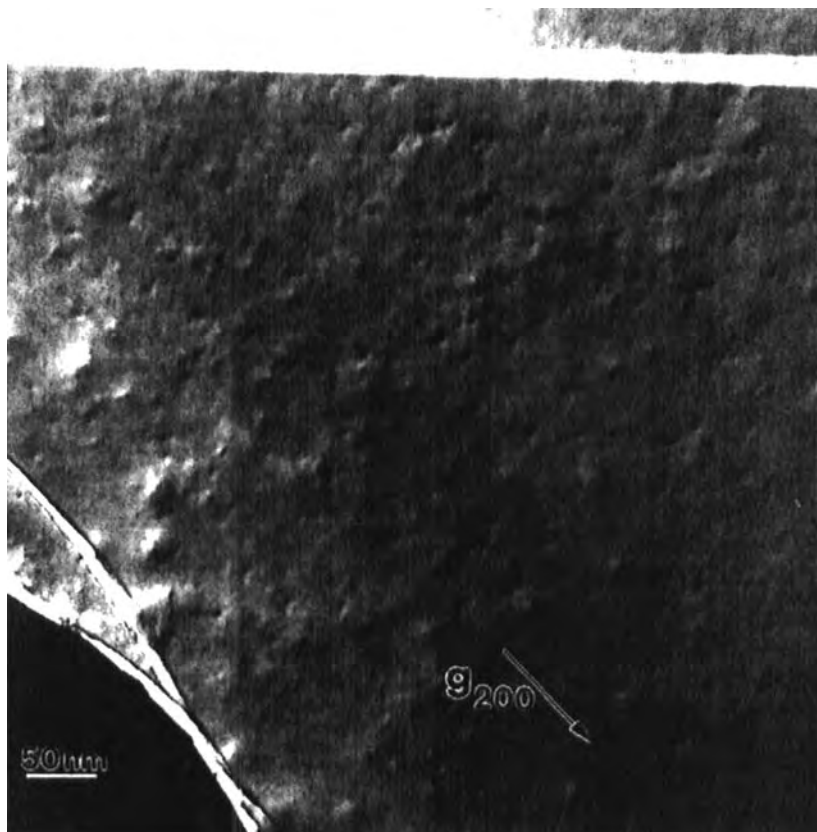
Typical dark-field TEM image showing defect cascades produced by 50 keV Kr^+. The defect cascades are imaged either as black–white contrast parallel to **g** or as black dot features. The length of the black–white interface or the diameter of the black dot can be used to measure the cascade diameter. A twin boundary is evident along the top portion of the image.

The extent of the strain field was measured to be roughly twice the diameter of the defect cascade. The strain field size is measured parallel to **g**; however, the end points for the measurement are somewhat arbitrary as the contrast from the defect cascade gradually blends into the background. The end points were chosen at about a 70% drop in the defect contrast and this was then compared with the actual size for that particular defect cascade. The end points for the actual size, measured perpendicular to **g**, are easy to determine as the contrast change is abrupt. A ratio of two was consistently found for different oxygen contents, irradiation directions and **g**-values used to form the dark-field image. Only defect cascades showing good black–white contrast from a strong two-beam condition were selected for strain field measurement.

The yield of defect cascades per incident ion was 50 ± 10% which is comparable with the values reported by Frischherz *et al.* (1993). Based on TEM calculations, nearly every ion will make a cascade in the first 30 nm, which raises the question of what happened to the other half of the defect cascades produced. The previous work

Statistics for the cascade size distribution in $YBa_2Cu_3O_x$ resulting from 50 keV Kr^+. Note the $[010]_a$ size was measured only for the $x = 6.9$ sample and the mean size was significantly larger than the other sizes. The subscript on the Miller indices for cascade size indicates the approximate direction of the incident ions.

Oxygen content	Size direction	Counts	Mean (nm)	Standard error (nm)
6·35	$[100]_c$	132	3·75	0·11
6·35	$[010]_c$	154	3·98	0·14
6·35	$[001]_a$	188	3·80	0·09
6·55	$[100]_c$	112	3·32	0·09
6·55	$[010]_c$	129	3·72	0·11
6·55	$[001]_a$	99	3·66	0·10
6·7	$[100]_c$	56	3·12	0·12
6·7	$[010]_c$	62	3·16	0·15
6·7	$[001]_a$	100	3·28	0·09
6·9	$[100]_c$	192	3·26	0·09
6·9	$[010]_c$	183	3·67	0·10
6·9	$[001]_a$	103	3·77	0·11
6·9	$[010]_a$	160	5·26	0·12

showed a HREM image of a defect cascade, suggesting partial recrystallization. This leads to the suggestion that about half the defect cascades may have fully recrystallized. Such a fully recrystallized defect cascade buried within a perfect lattice would be very hard to locate and image by either the dark-field or the HREM technique. Therefore it is not clear what remnants exist in a recrystallized defect cascade, but the local T_c may certainly be suppressed owing to oxygen disorder or deficiency.

A HREM image of a typical defect cascade is shown in Fig. 6. Other defects were located near the thin edge and also were found to have diameters between 3 and 4 nm. This is consistent with the data obtained from the dark-field measurements. The defoci of the image in fig. 6 is approximately −140 nm, as determined from the power spectrum taken from the sample's amorphous edge.

It is important to be aware that in HREM images the apparent size of a small object is a function of defocus owing to image delocalization (Marks 1984, 1985, Miller and Ewing 1993). A through-focal-image simulation series of an amorphous region surrounded by a square lattice shows how the apparent size of a defect will change with defocus (fig. 7). This effect is particularly important in the study of small particles, defect cascades, interfaces, etc.

Periodicities in the sample with a certain frequency will be displaced from their true location in the image. The amount of image delocalization is equal to the gradient of the contrast transfer function:

$$\nabla X(u) = 2\pi\lambda(\Delta z\, u + C_s\lambda^2 u^3), \tag{1}$$

where λ is the electron wavelength, u is a spatial frequency C_s is the spherical aberration coefficient and Δz is the objective defocus. The defocus at which there is no image delocalization is referred to as the overlap defocus, that is the image of the spacing in question overlaps its true location in the image. The overlap defocus is found by setting eqn. (1) equal to zero:

Fig. 3
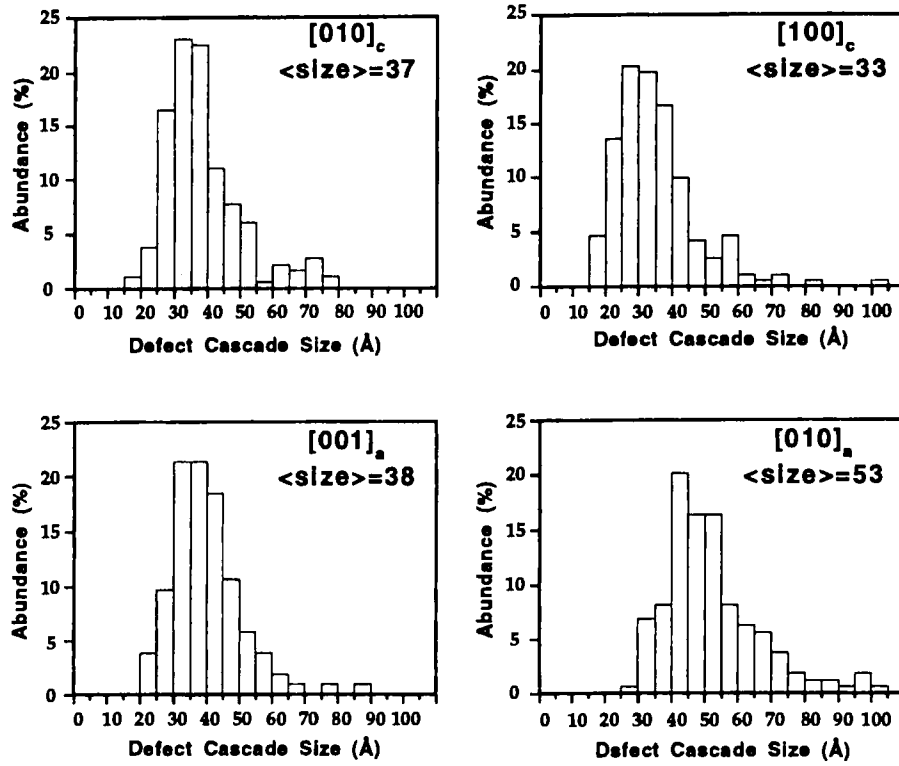
Defect cascade size distributions for the four different directions measured, holding oxygen constant at $x = 6.9$. Miller indices provide the measurement direction and the subscript indicates the axis near the irradiation direction. The $[100]_c$ and $[010]_c$ means are nearly the same, indicating a circular cross-section for cascades produced by irradiation near the c axis. The ratio of the $[010]_a$ and $[001]_a$ means is 1.6, indicating an elliptical cross section for cascades produced by irradiation near the a axis.

$$\Delta z = -\lambda^2 C_s u^2. \tag{2}$$

The overlap defocus for the 0.385 nm fringes seen in fig. 6 is -160 nm for 100 keV and $C_s = 1.7$ mm (Scherzer defocus, -80 nm). The effect of delocalization is a major problem for defoci near 0 nm; indeed the structure of the defect may become extremely obscured (see for instance fig. 7 (*b*)). Figures 7 (*b*)–(*i*) were generated by applying a contrast transfer function using linear imaging theory to the two-dimensional sample or object in fig. 7 (*a*). The lattice fringes are not parallel to the edges of the image; so the effects seen are not aliasing artefacts. Besides the obvious fringes seen in the amorphous region there is also a curving of the lattice image towards the centre. This could easily be seen in an experimental image and misinterpreted as an inwardly directed strain field, when it is merely an imaging artefact dependent on the defocus, for example, it is not seen in fig. 7 (*f*).

Fig. 4
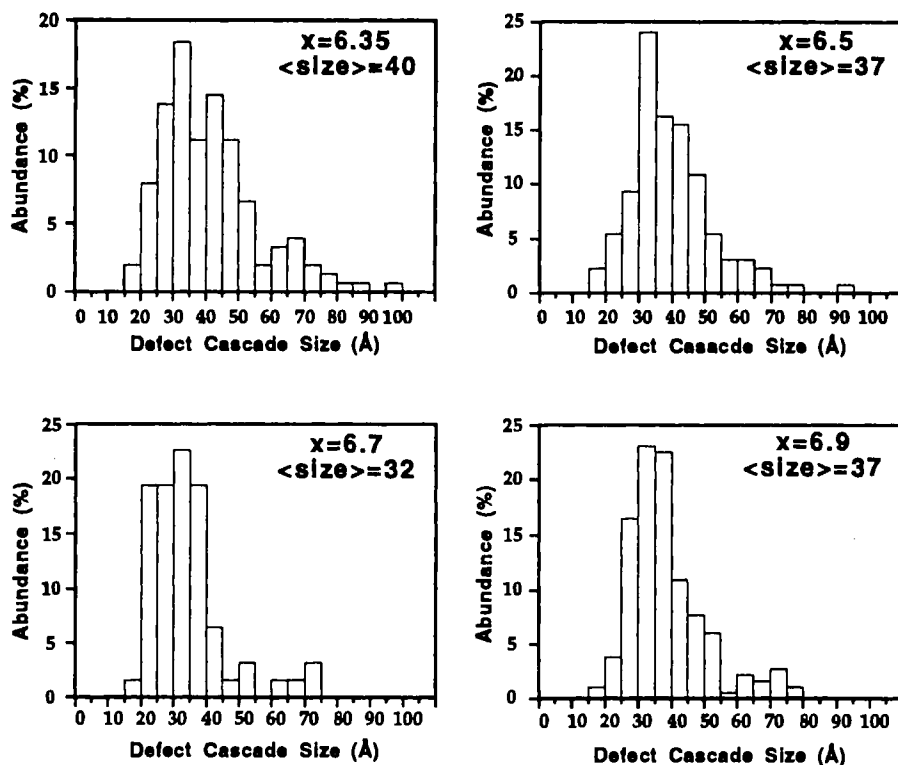
Defect cascade size distribution for the four different oxygen levels. All four distributions are for irradiation with 50 keV Kr^+ in YBCO near the c axis and measured in the [010] direction. The mean size is similar over this range of oxygen stoichiometry, which implies that the defect cascade size is independent of oxygen concentration.

Fig. 5
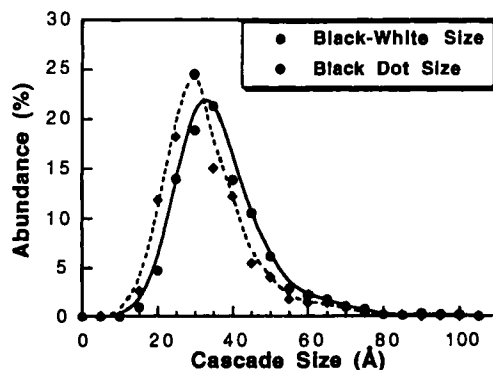
Size measurements were made on both black–white and black dot images for the defect cascades. The combined data for all four oxygen levels and all measurement directions, except $[010]_a$, are plotted for the black dot and black–white sizes. This was done to ensure that there was not a large effect on either the mean value or the shape of the distribution by measuring cascade sizes with one or the other type of image contrast. Both distributions are very similar in both mean and shape.

Fig. 6
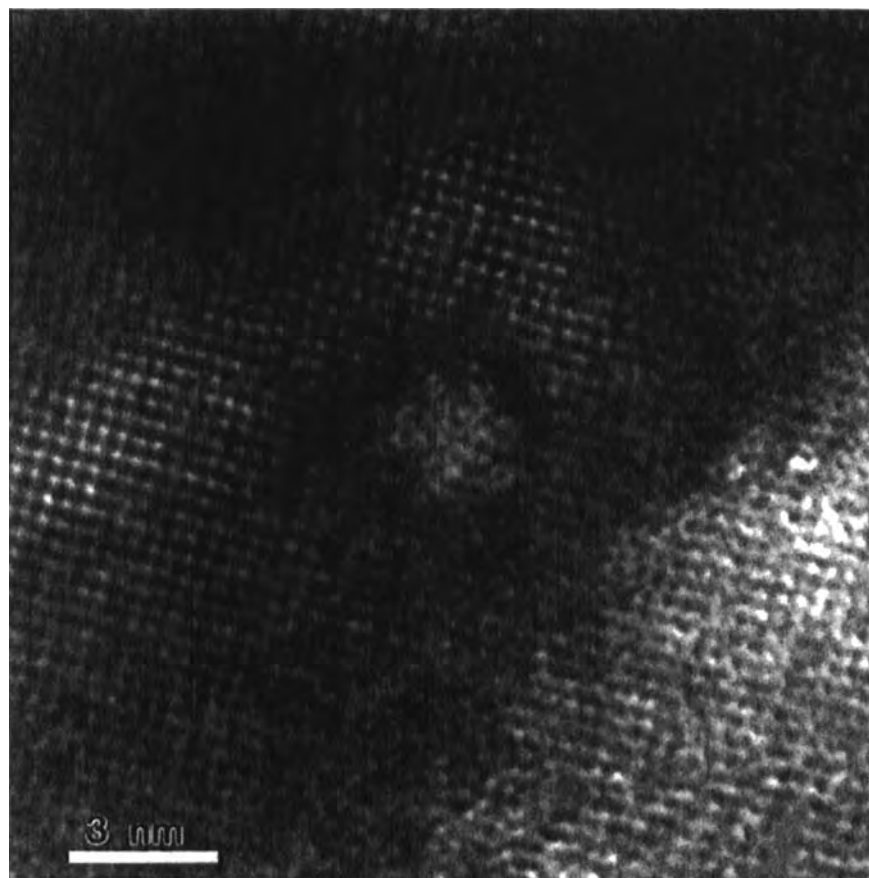
HREM image down the c axis of a $50\,keV\ Kr^+$ defect cascade in $YBa_2Cu_3O_{6\cdot35}$. The irradiation direction was near the c axis and, as the graphs in fig. 4 predict, the cascade cross-section is circular and about $3\cdot5\,nm$ in diameter. The objective defocus is about $-140\,nm$ under focus, which is close to the overlap defocus $(-160\,nm)$ for the $0\cdot385\,nm$ fringes at $100\,keV$ and a C_s of $1\cdot75\,mm$.

§ 4. Discussion

Defect cascade sizes produced by ions incident near the c axis in YBCO are relatively isotropic and independent of oxygen stoichiometry. For ions incident near the a axis the $[001]_a$ size was the same as that for the diameter of cascades produced by ions incident near c axis. For only the $x = 6\cdot9$ sample, the size along the $[010]_a$ direction was measured and was found to be $5\cdot5\,nm$. This elliptical cross-section for ions incident near the a axis and circular cross-section for ions incident near the c axis was reported for high-energy heavy-ion track damage in YBCO thin films and ceramics (Zhu *et al.* 1993). The fact that similar elliptical cross-sections are found in both types of damage suggests that an explanation based on a highly anisotropic thermal conductivity in these directions (a or b, c) is likely, as suggested by Zhu *et al.* That is, the defect size anisotropy is not related to the atomic recoil mechanisms (far different between the nuclear stopping at $50\,keV$ and the electronic

Fig. 7
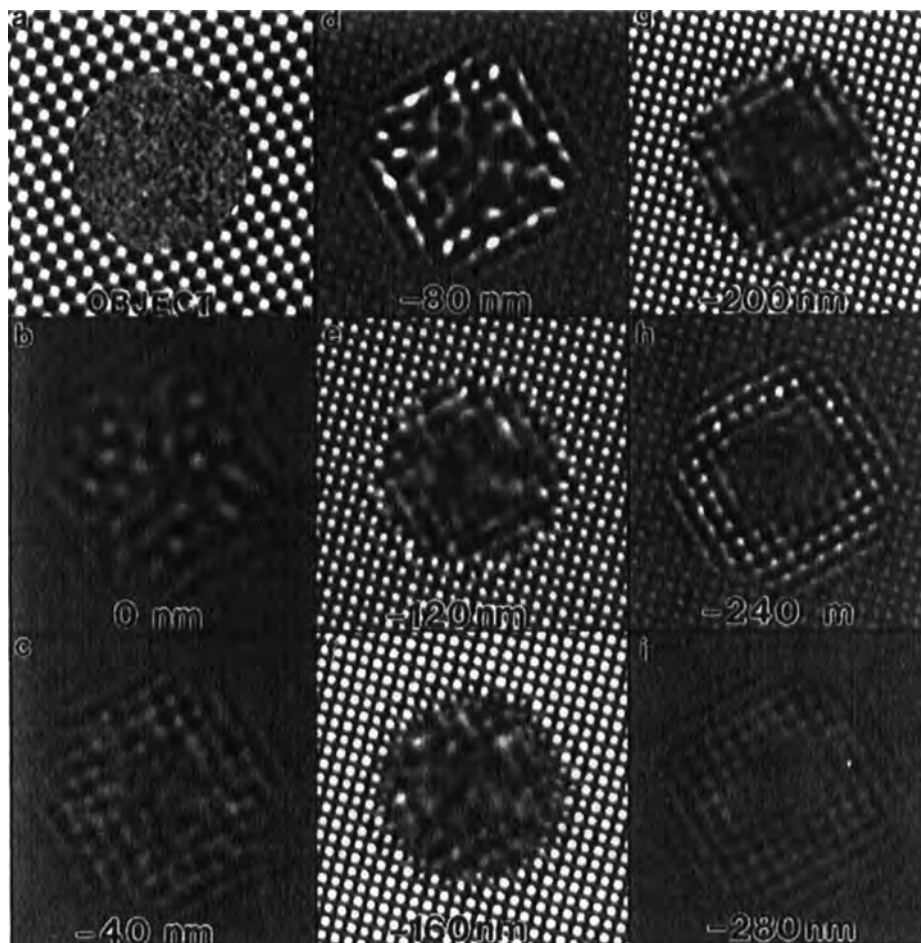
A simulated through focal series of the object in the top left corner (linear imaging theory). The object is intended to represent an amorphous cylinder surrounded by a square lattice; the lattice parameter is 0·385 nm. The objective defocus is indicated in each image. This series clearly shows two imaging artefacts dependent upon the defocus: the apparent size of the cylinder and a bending of the lattice fringes. Both of these effects are minimized at the overlap defocus (-160 nm).

stopping at several hundred megaelectronvolts) but to the dissipation of energy or cooling mechanism. However, we find the defect cascade size to be independent of oxygen content in contrast with reports by Zhu *et al.* that the diameter of heavy-ion track damage does vary with oxygen content.

A statistical analysis was performed on all the data to find any trends present. The standard error, that is the standard deviation divided by the square root of the counts, is presented in the table and a few trends are evident. If the crystallographic direction is held constant, then there is a $10 \pm 5\%$ increase in the mean from $x = 6\cdot9$ to $x = 6\cdot35$; this holds true for all three directions measured. A slight size anisotropy, $[100]_c \leqslant [010]_c$, can be seen by holding the oxygen stoichiometry constant. To con-

firm these trends, simultaneous 95% confidence intervals using Scheffé's procedure were determined. This procedure verified that any set of means different by at least 0·20 nm can be considered statistically significant in their difference. While these differences in the means are significant from a statistical point of view, the absolute differences in magnitudes are about 0·5 nm; thus there is little implication with regard to the magnetic flux-pinning properties.

The nearly uniform size of the defect cascades as a function of oxygen calls into question the explanation by Wisniewski *et al.* (1994) regarding the difference in flux pinning between the 60 and 90 K phases that had undergone neutron irradiation. They assumed a large cascade size difference (50%) between the two phases based on the theoretical work using low-energy (100–300 eV) ions by Kirsanov *et al.* (1993). Considering the defect cascades produced by the 50 keV Kr^+ irradiation should be similar to those produced by neutron radiation coupled with our uniform cascade size results; an explanation of flux-pinning behaviour for neutron radiation of samples with different oxygen stoichiometries should not be attributed to a variation in cascade size. The strain field size was nearly twice the cascade size for all oxygen contents. Thus, if one considers the strain field as the flux pinner, then the size is still not a function of oxygen.

§ 5. CONCLUSION

Irradiation of YBCO at various oxygen stoichiometries ($6·35 \leqslant x \leqslant 6·9$) with 50 keV Kr^+ produced defect cascade cross-sections that were found to be circular or elliptical depending upon the incident ion direction. The defect cascade size was constant for the four oxygen stoichiometries studied. This contradicts the interpretation by Wisniewski *et al.* (1994) in which a size variation in defect cascade size was assumed to explain flux-pinning behaviour in neutron-irradiated 60 and 90 K phase YBCO. Our size and yield measurements in the $x = 6·9$ crystals match those reported by Frischherz *et al.*

ACKNOWLEDGEMENTS

REFERENCES

ALLEN, C. W., FUNK, L. L., RYAN, E. A., and TAYLOR, A., 1989, *Nucl. Instrum. Meth.* B, **40–41**, 553.
ASHBY, M. F., and BROWN, L. M., 1963, *Phil. Mag.*, **7**, 1083.
BASU, S. N., ROY, T., MITCHELL, T. E., and NASTASI, M., 1989, *J. appl. Phys.*, **69**, 3167.
BUDHANI, R. C., ZHU, Y., and SUENAGA, M., 1992, *Appl. Phys. Lett.*, **61**, 985.
CIVALE, L., MARWICK, A. D., McELFRESH, M. W., WORTHINGTON, T. K., MALOZEMOFF, A. P., Holtzberg, F. H., THOMPSON, J. R., and KIRK, M. A., 1990, *Phys. Rev. Lett.*, **65**, 1164.
CIVALE, L., MARWICK, A. D., WORTHINGTON, T. K., KIRK, M. A., THOMPSON, J. R., KRUSIN-ELBAUM, L., SUN, Y., CLEM, J. R., and HOLTZBERG, F., 1991, *Phys. Rev. Lett.*, **67**, 648.
FRISCHHERZ, M. C., KIRK, M. A., FARMER, J., GREENWOOD, L. R., and WEBER, H. W., 1994, *Physica* C, **232**, 309.
FRISCHHERZ, M. C., KIRK, M. A., ZHANG, J. P., and WEBER, H. W., 1993, *Phil. Mag.* A, **76**, 1347.

GIAPINTZAKIS, J., LEE, W. C., RICE, J. P., GINSBERG, D. M., ROBERTSON, I. M., WHEELER, R., KIRK, M. A., and RUAULT, M. O., 1992, *Phys. Rev.* B, **45**, 10677.

HAGEN, S. J., WANG, Z. Z., and ONG, N. P., 1989, *Phys. Rev.* B, **40**, 9389.

KAISER, D. L., HOLTZBERG, F., CHISHOLM, M. F., and WORTHINGTON, T. K., 1987, *J. Cryst. Growth*, **85**, 593.

KIRK, M. A., 1993, *Cryogenics*, **33**, 235.

KIRK, M. A., BAKER, M. C., LIU, J. Z., LAM, D. J., and WEBER, H. W., 1988, Materials Research Society Symposium Proceedings, Vol. 99 (Pittsburgh, Pennsylvania: Materials Research Society), p. 209

KIRSANOV, V. V., MUSIN, N. N., and SHAMARINA, E. I., 1994, *Supercond. Phys. Chem. Technol.*, **7**, 412.

KIRSANOV, V. V., MUSIN, N. N., and SHAMARINA, H. J., 1992, *Phys. Lett.* A, **171**, 223; 1993, *Ibid.*, **182**, 169.

KIRSANOV, V. V., MUSLIN, N. N., ROSKIN, D. G., and SHAMARINA, E. I., 1993, *Cryogenics*, **33**, 477.

LESSURE, H. S., SIMIZU, S., SANKAR, S. G., McHENRY, M. E., COST, J. R., and MALEY, M. P., 1991, *J. appl. Phys.*, **70**, 6513.

MARKS, L. D., 1985, *Ultramicroscopy*, **18**, 33. 1984, *Ibid.*, **12**, 237; 1995, *Ibid.* (to be published.

MARKS, L. D., LI, D. J., SHIBAHARA, H., and ZHANG, J. P., 1988, *J. Electron Microsc. Technique*, **8**, 297.

MILLER, M. L., and EWING, R. C., 1993, *Ultramicroscopy*, **48**, 203.

SALDIN, D. K., STATHOPOULOS, A. Y., and WHELAN, M. J., 1979, *Phil. Trans. R. Soc.* 292, 523.

SHAO-CHUN, C., DONG-MING, Z., DIAN-LIN, Z., DUAN, H. M., and HERMANN, A. M., 1991, *Phys. Rev.* B, **44**, 12571.

ST LOUIS-WEBER, M., DRAVID, V. P., and BALACHANDRAN, U., 1995, *Physica* C, **243**, 273.

VAN TENDELOO, G., and AMELINCKX, S., 1988, *J. Electron Microsc. Technique*, **8**, 285.

VEAL, B. W., PAULIKAS, A. P., YOU, H., SHI, H., FANG, Y., and DOWNEY, J., 1990, *Phys. Rev.* B, **42**, 6305.

VETRANO, J. S., 1990, PhD Thesis, University of Illinois at Urbana-Champaign.

VLECK, B. M., FRISCHHERZ, M. C., FLESHLER, S., WELP, U., LIU, J. Z., DOWNEY, J., VANDERVOORT, K. G., CRABTREE, G. W., KIRK, M. A., GIAPINTZAKIS, J., and FARMER, J., 1992, *Phys. Rev.* B, **46**, 6441.

WHEELER, R., KIRK, M. A., MARWICK, A. D., CIVALE, L., and HOLTZBERG, F. H., 1993, *Appl. Phys. Lett.*, **63**, 1573.

WILKENS, M., 1970, *Modern Diffraction and Imaging Tecniques in Material Science*, Vol. 1, edited by S. Amelinckx, R. Gevers, G. Remaut, and J. Van Landuyt (Amsterdam: North-Holland), p. 233.

WISNIEWSKI, A., BRANDSTATTER, G., CZURDA, C., WEBER, H. W., MORAWSKI, A., and LADA, T., 1994, *Physica* C, **220**, 181.

ZHU, Y., BUDHANI, R. C., CAI, Z. X., WELCH, D. O., SUENAGA, M., YOSHIZAKI, R., and IKEDA, H., 1993, *Phil. Mag. Lett.*, **67**, 125.